Contents list available at CBIORE journal website

International Journal of Renewable Energy Development

Journal homepage: https://ijred.cbiore.id

Research Article

Continuous closed-circuit removal of methylene blue and methyl orange dyes by activated Pomelo peel biochar alginate hydrogel beads

Mai Lien Tran*

Institute of Environmental Science, Engineering and Management, Industrial University of Ho Chi Minh City, Ho Chi Minh City, Vietnam

Abstract. The successful fabrication of composite hydrogel beads was realized through the integration of activated pomelo peel biochar (PBC) into a sodium alginate (NaAlg) polymeric matrix, a process facilitated by Ca^{2+}-induced ionic cross-linking. Morphological evaluations of the resulting material confirmed a highly textured surface, demonstrating that the PBC particles were effectively and uniformly embedded within the alginate framework. In terms of performance, the composite formulation consisting of 3.3% (w/v) PBC and NaAlg exhibited exceptional adsorption affinity for both methylene blue (MB) and methyl orange (MO) dyes. The equilibrium data showed a superior fit to the Langmuir isotherm model, which implies a predominantly homogeneous monolayer adsorption process; under continuous flow conditions at 30°C, the maximum adsorption capacities were recorded at 279.68 mg/g for MB and 179.02 mg/g for MO. Furthermore, kinetic modeling indicated that the adsorption behavior strictly followed a pseudo-second-order mechanism, suggesting that the rate-limiting step is governed by chemisorption rather than physical forces alone. The fundamental removal mechanism is believed to be a synergistic interplay of various physicochemical forces, including pore-filling within the biochar structure, π-π interactions between aromatic rings, and the formation of hydrogen bonds between the dye molecules and the composite surface..

Keywords: Activated pomelo peel biochar; bead composite; flow-continuous adsorption; methylene blue; methyl orange

Received: 5th March 2026; Revised: 28th June 2026; Accepted: 15th July 2026; Available online: 4th August 2026

1. Introduction

Accelerating global industrialization has intensified the freshwater crisis through the discharge of inadequately treated effluents into aquatic ecosystems. Among the various classes of contaminants, dyes are particularly prevalent due to their extensive utilization in the textile, pharmaceutical, food, paper, and cosmetic sectors (Maheshwari *et al.* 2021, Jorge *et a*l. 2023). As highly water-soluble compounds, these dyes easily infiltrate aquatic bodies, posing significant ecological threats (Akter *et al.* 2023, Islam *et al.* 2023, Lin *et al.* 2023). Apart from their aesthetic impact, dyes elevate water turbidity, which blocks sunlight penetration and suppresses photosynthesis in aquatic ecosystems. Furthermore, many dyes, specifically those characterized by azo groups and complex aromatic structures, are associated with severe health risks, including carcinogenic and mutagenic properties. Because of their chemical stability and non-biodegradability, these pollutants persist in ecosystems, making the development of robust remediation technologies a critical environmental priority.

To address the challenge of dye-laden effluents, a variety of physical, chemical, and biological remediation strategies have been developed(Al-Tohamy *et al.* 2022, Solayman *et al.* 2023). Physical techniques, such as membrane filtration, ion exchange, and adsorption, remain widely utilized due to their effectiveness in removing various dyes (Liu 2020, Soltani *et al.* 2021, Kumari *et al.* 2023). For instance, methylene blue and eriochrome black T, malachite green, and crystal violet (Subrahmanya *et al.* 2022, Wu *et al.* 2023) were removed effectively by modified membranes. Both basic and acidic dyes could be eliminated by ion-exchange microbeads (Lu *et al.* 2022). Chemical methods (e.g., coagulation, ozonation) and photocatalysis offer high dye-removal efficiency, but they are often constrained by excessive chemical consumption and secondary pollutant generation (Bal and Thakur 2022, Haleem *et al.* 2023). Similarly, biological treatments provide an eco-friendly and cost-effective alternative (Rathi and Kumar 2022) but suffer from slow removal rates and strict operational or enzymatic requirements (Kathing and Saini 2022). Consequently, adsorption has emerged as a preferred approach owing to its superior efficiency, operational simplicity, and economic feasibility (Yagub *et al.* 2014, Shi *et al.* 2022, Al-Asadi *et al.* 2025).

In the sorption method, various materials, including activated carbon, chitosan-based composites, and metal oxides, have been extensively employed for the remediation of dyes and other aqueous pollutants (Agarwala and Mulky 2023, Hosny *et al.* 2023, Bellaj *et al.* 2024). Recently, research efforts have increasingly pivoted toward the synthesis of low-cost adsorbents derived from agricultural by-products and waste materials to enhance economic sustainability (Al-Gheethi *et al.* 2022, Haque *et al.* 2022, Nayagam and Prasanna 2022). However, prepared biochars presented relatively low adsorption capacities; specifically, adsorbents synthesized from banana stem waste achieved maximum uptake capacities of 15.22 mg/g for methylene blue and 24.08 mg/g for basic fuchsin (Das *et al.* 2023). To enhance the adsorption performance, multiple biochars have been synthesized with modifications (Saravanan *et al.* 2023, Li *et*

* Corresponding author: tranmailien@iuh.edu.vn (M.L.Tran)

https://doi.org/10.61435/ijred.2026.62466
ISSN: 2252-4940/© 2026.The Author(s). Published by CBIORE

al. 2024). Among those, biochars from pomelo peel under the activations were investigated as excellent adsorbents with the highest adsorption capacity for methylene blue and oxytetracycline up to 385.11 and 95.6 mg/g, respectively (Tran 2025, Tran *et al*. 2025). Even though their practical implementation is often hindered by their typical powder form. In large-scale operations, powdered adsorbents are prone to excessive dispersion, leading to significant challenges and high costs associated with their separation and recovery from treated effluents. Consequently, immobilizing these materials onto a stable and suitable structural platform represents a critical strategy to overcome these technical limitations and facilitate their industrial application.

Alginate, a naturally occurring polysaccharide, is widely recognized for its non-toxicity and inherent biodegradability. A key functional characteristic of alginate is its ability to undergo gelation in the presence of divalent cations, such as Ca^{2+}, through the formation of an egg-box structural model (Makarova *et al*. 2023). Regarding this property, nanomaterials can be effectively entrapped within an alginate hydrogel matrix to develop advanced composite adsorbents. In this study, biochar derived from pomelo peel and activated via phosphoric acid (PBC) was immobilized in alginate beads to become potential adsorbents. The synthesized PBC-alginate beads were applied in removing Methylene Blue (MB) and Methyl Orange (MO), representing cationic and anionic dye models, respectively, under continuous-flow conditions. This configuration overcomes the mass transfer limitations of conventional batch and fixed-bed systems by maintaining a maximized, steady concentration driving force through dynamic fluid recirculation (Biswas *et al*. 2020). By separating effluent breakthrough limits from bed saturation, this design allows the adsorbent matrix to consistently operate near its ultimate theoretical capacity. Furthermore, the recycling loops eliminate severe pressure drops inherent to long fixed beds, while facilitating seamless, in-situ regeneration without process downtime. The structural and chemical properties of the composite beads were studied using X-ray diffraction (XRD), Fourier-transform infrared spectroscopy (FTIR), and scanning electron microscopy (SEM). Concurrently, the adsorption isotherms and kinetic profiles were systematically analyzed to determine the uptake capacity and propose adsorption mechanisms.

2. Materials and methods

2.1. Materials

Methylene blue (MB, $C_{16}H_{18}ClN_3S$), methyl orange (MO, $C_{14}H_{14}N_3NaO_3S$), phosphoric acid (H_3PO_4), sodium hydroxide (NaOH), hydrochloric acid (HCl), and sodium alginate [$(C_6H_7NaO_6)_n$] were sourced from the supplier Xilong Scientific in Shantou, China. All solutions were prepared using deionized (DI) water.

2.2. Preparation of biochar bead

The H_3PO_4-activated pomelo peel biochar (PBC) was synthesized following the protocol established in our previous work (Tran 2025). Specifically, pomelo peel powder was thoroughly blended with 85% H_3PO_4 at a 1:5 w/v ratio before undergoing thermal pyrolysis at 700 °C (heating rate of 15°C/min) for 1 hour. Following ambient cooling, the resulting product was rinsed with deionized water until neutrality and dried overnight at 60°C. To prepare the composite beads, 6.0 g of sodium alginate was completely dissolved in 90 mL of deionized (DI) water under constant stirring at 50 °C for 30 min. Subsequently, varying mass/volume fractions of PBC (0, 2.0, 3.3, and 5.3% w/v) were incrementally introduced into the alginate matrix. The resulting suspensions, designated as NaAlg, PBC2.0@NaAlg, PBC3.3@NaAlg, and PBC5.3@NaAlg, respectively, were stirred for an additional 30 min. To ensure structural homogeneity, the mixtures underwent ultrasonication for 30 min to eliminate entrapped air bubbles. Finally, the slurries were dispersed dropwise into a 1 M $CaCl_2$ solution to form beads. The fabricated beads were harvested, rinsed thoroughly with DI water to remove residual ions, and stored in a hydrated state for subsequent experiments.

2.3. Characterization

The surface morphology and textural characteristics of the synthesized composite beads were examined using scanning electron microscopy (SEM, S-4800, Hitachi, Tokyo, Japan). To elucidate the crystalline structure and phase composition, X-ray diffraction (XRD) patterns were recorded on a Shimadzu LabX XRD-6100 diffractometer (Tokyo, Japan). Furthermore, the evolution of surface functional groups was identified via Fourier transform infrared spectroscopy (FT-IR), conducted on a PerkinElmer Spectrum 10.5.2 instrument (Bucks, England) within a specified spectral range.

2.4. Adsorption experiments

The adsorption performance of the synthesized beads toward MB and MO dyes was evaluated using the column batch experiment (Fig. 1). Continuous-flow adsorption was conducted in a closed-loop system using a 2.0 cm inner diameter glass column packed with adsorbent to a height of 5.0 cm (bed volume V_b = 15.71 cm^3). A 100.0 mL dye solution was continuously recirculated at a fixed flow rate of 40.0 mL/min, yielding an empty bed contact time of 0.393 min and a total hydraulic retention time of 2.5 min. Supported by inert glass wool, the uniformly wet-packed bed maintained stable flow (2% deviation) with a negligible pressure drop. At predetermined time intervals, aliquots were withdrawn from the reservoir to determine the residual dye concentration. Quantitative analysis was performed via an ultraviolet-visible spectrophotometer (Genesys 10S, Thermo Scientific, Madison, WI, USA) at maximum absorption wavelengths of 665nm for MO and 465 nm for MO.

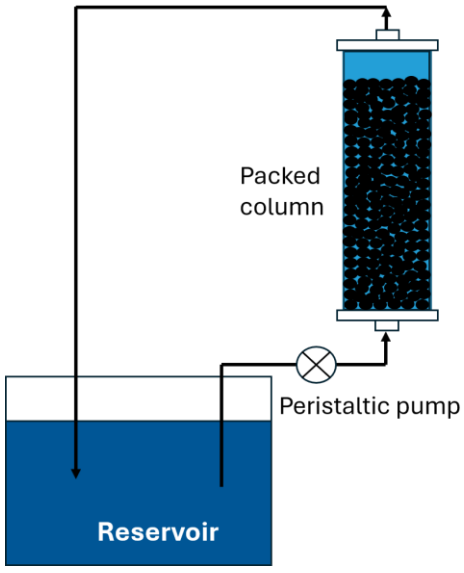

Fig. 1. Scheme of the column batch adsorption

The dye removal efficiency (R, %) was calculated using the following relationship:

$$R(\%) = \frac{(C_0 - C_t)}{C_0} \times 100 \quad (1)$$

where C_0 and C_t (mg/L) denote the dye concentration at the initial state and at time t (min), respectively.

The adsorption capacity (q_t, mg/g) was determined based on the equation:

$$q_t = \frac{(C_0 - C_t) \times V}{m} \quad (2)$$

where V (L) represents the total volume of the aqueous solution and m (g) is the dry weight of the adsorbent beads utilized in the column.

2.5. Adsorption isotherm

The equilibrium adsorption isotherms for MB and MO onto the synthesized beads were established at 30 °C. Specifically, dye solutions with initial concentrations varying from 100 to 2000 mg/L were introduced into the fixed-bed column at a consistent flow rate of 40 mL/min. Upon reaching equilibrium, the remaining dye concentrations were analyzed using the spectrophotometric method described previously.

To evaluate the interaction mechanisms and distribution of dye molecules on the adsorbent surface, the experimental data were fitted using five well-established isotherm models: Langmuir, Freundlich, Temkin, and Dubinin-Radushkevich (D-R) (Al-Ghouti and Da'ana 2020). The mathematical expressions for these models are defined as follows:

Langmuir isotherm equation:

$$q_e = \frac{q_m K_L C_e}{1 + K_L C_e} \quad (3)$$

Freundlich isotherm equation:

$$q_e = K_F C_e^{1/n_F} \quad (4)$$

Temkin isotherm equation:

$$q_e = \frac{RT}{b_T} ln\, a_T\, C_e \quad (5)$$

DR isotherm equation:

$$q_e = q_{DR}\, exp\left(\frac{(RT\, ln(1 + 1/C_e))^2}{-2E^2}\right) \quad (6)$$

where:

- q_e (mg/g) is the equilibrium adsorption capacity, and C_e (mg/L) is the equilibrium concentration.
- q_m and q_{DR} (mg/g) represent the maximum adsorption capacities for the Langmuir and D-R models, respectively.
- K_L (L/mg) represents the Langmuir affinity constant, K_F ((mg/g)(L/mg)$^{1/n}$) is the Freundlich constant related to adsorption capacity, and n_F (dimensionless) is the heterogeneity factor indicating the adsorption intensity.
- a_T (L/g) is the Temkin isotherm equilibrium binding constant, b_T (J/mol) is the Temkin constant related to the heat of sorption, R is the ideal gas constant (8.314 J/mol.K), and T (K) is the absolute temperature.
- E (kJ/mol) represents the mean free energy of adsorption per mole of the adsorbate.

2.6. Thermodynamics of adsorption

To understand the character of the sorption process, the experiments were carried out at different temperatures (303 – 323 K) to determine the thermodynamic parameters of the sorption process. The free energy change (ΔG^0, kJ/mol), enthalpy change (ΔH^0, kJ/mol), and entropy change (ΔS^0, J/mol.K) were calculated by the following equations:

$$log\left(\frac{C_{e,S}}{C_{e,L}}\right) = \frac{\Delta S^0}{2.303R} + \frac{-\Delta H^0}{2.303RT} \quad (7)$$

$$\Delta G^0 = \Delta H^0 - T\Delta S^0 \quad (8)$$

where $C_{e,S}$ and $C_{e,L}$ (mg/L) are adsorbent concentrations on solid phase and liquid phase. The slope and intercept of the plot between $log\left(\frac{C_{e,S}}{C_{e,L}}\right)$ and $\frac{1}{T}$ yield the magnitude of enthalpy change (ΔH^0) and entropy change (ΔS^0). The value of the Gibbs free energy change was calculated at different temperatures using Equation 8.

2.7. Adsorption kinetics

Adsorption kinetics of MB and MO onto the synthesized beads were evaluated at initial concentrations of 300 and 400 mg/L, respectively. Aliquots were extracted and analyzed at predetermined time intervals until equilibrium was established. To describe the adsorption mechanism, four kinetic models, including Pseudo first-order (PFO), Pseudo second-order (PSO), Elovich, and intraparticle diffusion, were studied. The nonlinear mathematical forms are detailed in equations (9) through (12).

$$q_t = q_e(1 - e^{-k_1 t}) \quad (9)$$

$$q_t = \frac{q_e^2 k_2 t}{1 + q_e k_2 t} \quad (10)$$

$$q_t = \frac{1}{\beta} ln(\alpha\beta) + \frac{1}{\beta} ln\, t \quad (11)$$

$$q_t = k_{ip} t^{0.5} + C_{ip} \quad (12)$$

In these expressions, q_t and q_e (mg/g) denote the adsorption capacities at time t (min) and at equilibrium, respectively. The rate constants are represented by k_1 (min^{-1}), k_2 (g/mg.min), and k_{id} (mg/(g.min$^{0.5}$)) while α (mg/g.min) and β (g/mg) signify the initial adsorption rate and the desorption related to chemisorption. The term C_{id} represents the intraparticle diffusion intercept.

3. Results and discussion

3.1. Characterizations

General physical properties of the synthesized hydrogel composites are summarized in Table 1. A positive correlation was observed between the PBC loading and both the wet and dry mass of the samples. This trend is attributed to the integration of high-density biochar particles within a consistent matrix volume. Conversely, the inclusion of PBC led to a reduction in moisture content relative to the pristine NaAlg beads. Furthermore, the bead diameters remained relatively uniform, ranging from 2.5 to 2.6 mm, which suggests that the bulk volume was not significantly altered by the varying PBC percentages.

To assess the crystalline structure of composite materials, X-ray diffraction analysis was performed on PBC, NaAlg, and PBC3.3@NaAlg hybrid (Fig. 2). The XRD profile for the NaAlg beads is characterized by several prominent and sharp reflections centered at 2θ values of 31.8°, 45.4°, 66.4°, and 75.4° (Faried *et*

Table 1.
General properties of NaAlg and composites with different PBC loading

Material	Diameter (*mm*)	Wet weight (*g*)	Dry weight (*g*)	Moisture content (*%*)
NaAlg	2.6	6.95	0.3750	94.60432
PBC2.0@NaAlg	2.5	7.0756	0.6376	90.98875
PBC3.3@NaAlg	2.6	7.1785	0.6465	90.99394
PBC5.3@NaAlg	2.6	7.2123	0.6554	90.91275

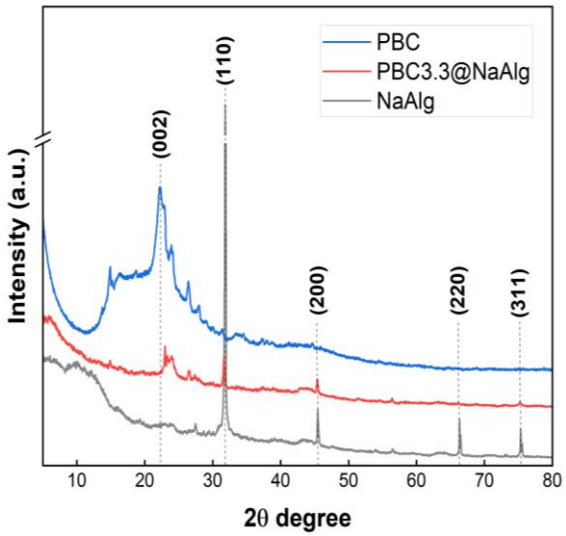

Fig. 2. XRD patterns of PBC, NaAlg, and PBC-NaAlg composite

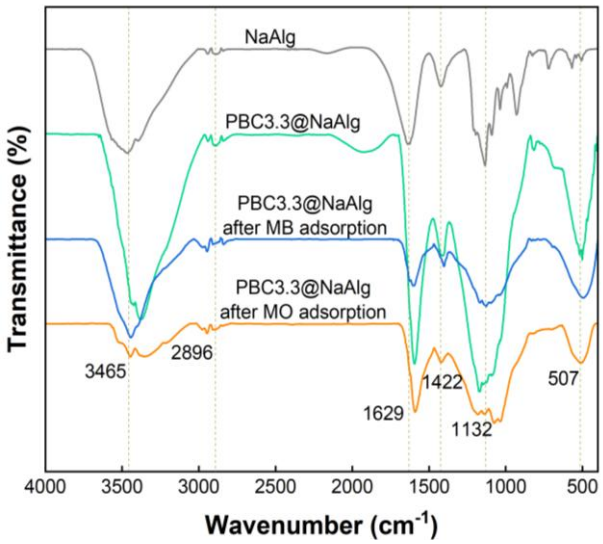

Fig. 3. FTIR spectra of NaAlg, hybrid bead before and after adsorption

al. 2016, Liao *et al*. 2018). These well-defined reflections indicate a relatively high degree of crystallinity within the alginate matrix, likely resulting from the ordered arrangement of polymer chains during the bead formation process. In contrast, the PBC profile shows broader, less intense peaks, particularly in the 20 to 30° range. This is a signature of amorphous carbon structures with localized graphene-like domains, typical for biochar produced through carbonization (Tran 2025). Following the incorporation of the biochar, the PBC3.3@NaAlg spectrum exhibits a drastic reduction in the intensity of a prominent, sharp crystalline reflection at $2\theta = 31.8°$, while a broad amorphous halo emerges in the 2θ = 15° - 25° region. This substantial attenuation of crystalline peak intensity, coupled with the significant baseline broadening, quantitatively demonstrates that the embedding of disordered PBC particles effectively disrupts the long-range coordination of the alginate matrix, driving the composite toward a predominantly amorphous state.

The FTIR spectra of NaAlg and PBC-NaAlg composite are presented in Fig. 3. For the pristine NaAlg, the broad absorption band observed between 3300 and 3500 cm^{-1} is characteristic of –OH stretching vibrations, a hallmark of the sodium alginate structure (Zhao *et al*. 2024). The signal at 2896 cm^{-1} is attributed to C–H stretching in aliphatic carbon atoms. Furthermore, the peaks identified at 1635 cm^{-1} and 1422 cm^{-1} correspond to the asymmetric and symmetric stretching of the carboxylate groups (C=O and C–O), respectively. The complex region between 1000 and 1100 cm^{-1} is assigned to C–O and C–O–C stretching, typically of the ring in the alginate matrix. Comparing with NaAlg, the spectrum of PBC3.3@NaAlg reveals a distinct broadening of the O–H, C=O, C–O, and C–O–C bands, suggesting a distribution of hydrogen bonding environments, likely due to the varied oxygen-containing groups (phenolic, carboxylic) on the biochar surface. The shift and intensity variation of the broad band at 3465 cm^{-1} and the characteristic peaks at 1635 cm^{-1} and 1422 cm^{-1} upon composite formation confirm the establishment of hydrogen bonding and electrostatic cross-linking between the sodium alginate matrix and the functional groups of the biochar. Following the adsorption of MB and MO dyes, the notable perturbations and intensity changes within the fingerprint region 1132 - 507 cm^{-1} demonstrate that these oxygen-containing functional groups serve as active primary binding sites. Specifically, the pathway governing dye immobilization is driven by a synergistic combination of electrostatic attractions between the anionic carboxylate groups of the composite and cationic dye molecules, alongside π-π electron donor-acceptor interactions involving the aromatic framework of the biochar. In addition, the absorption near 500 cm^{-1} in the PBC3.3@NaAlg spectrum is linked to P-O stretching vibrations, formed in the biochar activation process (Tran 2025). Post-adsorption, this peak broadened further, likely due to the spectral overlap with C-N-C vibrations inherent in the molecular structure of the adsorbed dyes. All shifting and assignment of characteristic FTIR bands for the composite before and after MB and MO adsorption have been summarized in Table 2.

The morphological characteristics of NaAlg and PBC3.3@NaAlg beads were elucidated through SEM analysis. Observations indicate a clear topographical divergence between the pristine NaAlg bead (Fig. 4a) and the PBC3.3@NaAlg composite (Fig. 4b). The surface of the NaAlg bead displays a consolidated, dense macro-aggregation where the structural boundaries are partially smoothed over, yielding lower apparent porosity and localized topographic flattening. In contrast, the PBC3.3@NaAlg surface demonstrates a highly exfoliated, coralloid texture with an extensively developed

Table 2.
FTIR peak assignments of PBC3.3@NaAlg composite before and after dye adsorption

Vibration	PBC3.3@NaAlg (cm^{-1})	After MB adsorption (cm^{-1})	After MO adsorption (cm^{-1})	Shift significance
–OH stretching	3381	3465	3465	Out-of-plane hydrogen bonding and surface complexation with dye molecules.
–CH stretching	2896	2941	2941	Involvement of aliphatic structures from the biochar matrix.
Asymmetric $–COO^-$ stretching	1629	1596	1584	Major electrostatic interaction site for MB dye and hydrogen bonding.
Symmetric $–COO^-$ stretching	1422	1400	1412	Participation of alginate carboxylate groups in coordination/binding.
–C-O –C-O-C stretchings	1171	1132	1082	Oxygen-containing functional groups act as adsorption active sites.
Aromatic –CH out-of-plane bending	507	490	501	π-π electron donor-acceptor interactions between biochar aromatic rings and dye structures.

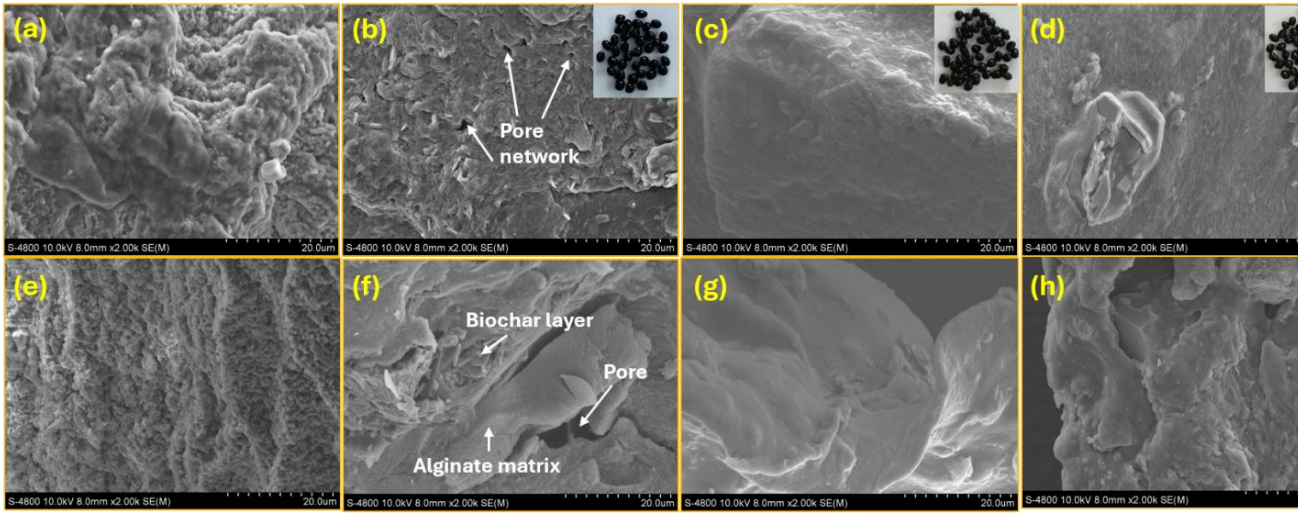

Fig. 4. SEM images of NaAlg and PBC3.3@NaAlg bead surfaces (a–d) and cross-sections (e–h) before and after MB and MO adsorption

network of uniformly distributed open pores ranging from 1.0 to 3.0 μm in diameter. This multi-layered, exfoliated arrangement drastically elevates the surface roughness and effectively suppresses tight particle agglomeration. Consequently, the structural framework of the PBC3.3@NaAlg provides a more accessible spatial geometry and higher active surface exposure, which is advantageous for mass transfer dynamics. Furthermore, cross-sectional SEM images reveal fundamentally different internal frameworks for the two materials. The internal structure of the NaAlg bead (Fig. 4e) is a highly ordered, pleated, and lamellar internal structure. Conversely, the PBC3.3@NaAlg cross-section (Fig. 4f) displays a heterogeneous internal layout dominated by large, asymmetric macro-pores exceeding 10.0 μm in diameter alongside localized crystalline block inclusions. Instead of continuous layers, it consists of sharp, angular crystalline-like blocks embedded within a disorganized matrix. This suggests the formation of a composite between NaAlg and biochar. After adsorption of MB and MO processes, the surface undergoes a visible transformation, appearing significantly smoother (Fig. 4c,d). The previously distinct crevices and valleys have been largely filled or obscured, and adsorbate molecules have successfully occupied the available pore volume and settled within the surface irregularities. This smoothing effect is also evident in the cross-sectional SEM images (Fig. 4g,h). The once sharp-edged internal fragments appear encapsulated or masked by a secondary layer, confirming that the adsorbates successfully permeated the particle core and adhered to internal active sites.

3.2. Adsorption of MB and MO on different beads

The adsorptive performance of the synthesized composite beads was evaluated as a function of PBC loading, with the removal efficiency for MB and MO illustrated in Fig. 5a and Fig. 5b, respectively. The data illustrate a significant enhancement in adsorption performance through the hybridization of sodium alginate and biochar. While NaAlg bead exhibits a relatively poor removal (only 28.4% for MB and 3.0% for MO after 600-min adsorption), the incorporation of PBC facilitates a dramatic shift in the kinetic profile, characterized by a rapid initial uptake within the first 60 minutes. Specifically, 89.5% of MB and 87.6% of MO were removed by PBC2.0@NaAlg, which containted 2.0% w/v of PBC, respectively. Increasing the biochar weight fraction correlated positively with pollutant removal. Particularly, MB removal climbed from 89.5% to 97.3% as the PBC content increased from 2.0 to 5.3, while MO removal reached a peak of 98.3%. In comparison with MO, MB could be removed by NaAlg bead due to the presence of the carboxylate (COO^-) (Lu *et al.*

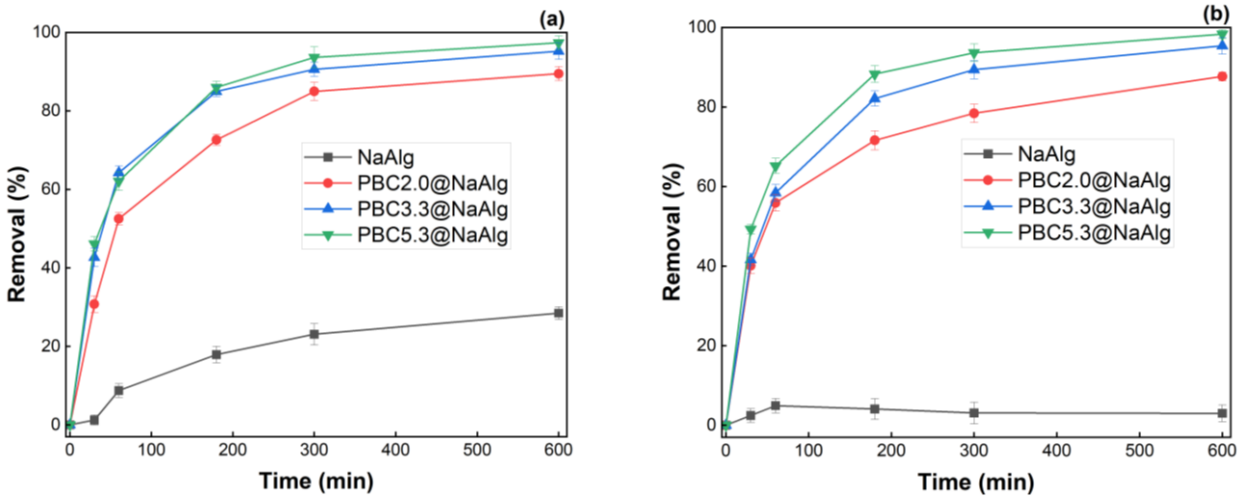

Fig. 5. Removal of MB (a) and MO (b) by different beads. Experimental parameters: $[MB]_{inital}$ = 300 mg/L, $[MO]_{inital}$ = 400 mg/L, natural pH

2021), which facilitates electrostatic interactions with cationic MB molecules while exhibiting negligible affinity for anionic MO species. When biochar was introduced, morphological modifications resulting from biochar integration (as shown in Figs. 4b,f) expanded the accessible surface area and promoted the intra-particle diffusion of dye molecules. Furthermore, the synergistic interaction between the dyes and the composite is reinforced by the presence of aromatic frameworks and functional groups, including -COOH, -OH, and C=C on the biochar surface, which provide active sites for complexation and π–π stacking.

3.3. Effect of pH on dye adsorption

The effect of initial solution pH was investigated across a range of 3 to 9 due to the stability of beads (Stachowiak *et al.* 2023). As illustrated in Fig. 6, the adsorption performance exhibited negligible fluctuations despite variations in pH. Specifically, removal efficiencies for MB and MO remained consistently high, ranging between 95% and 98%. Within the investigated pH range, MB exists predominantly in cationic form, whereas MO is primarily anionic. The adsorbent beads were composed of biochar activated by phosphoric acid with a negative charge in the pH range from 2 to 12 (Tran 2025) and calcium-crosslinked alginate characterized by negatively charged carboxylate groups. The specific result for determining the point of zero charge of PBC3.3@NaAlg beads is shown in Fig. 7. Despite the predominantly negative surface charge of the beads, they demonstrated high uptake capacity for the similarly charged MO molecules. This phenomenon indicates that electrostatic interactions are not the primary mechanism governing the adsorption process. This persistent uptake provides strong physicochemical justification that the adsorption is driven by dominant non-electrostatic interactions, specifically π-π electron donor-acceptor interactions between the aromatic rings of MO and the carbon matrix, alongside hydrogen bonding with surface functional groups. These strong physical-chemical affinities easily overcome the weak electrostatic repulsion, facilitating effective single-layer coverage as confirmed by the Langmuir model fitting. The sustained high removal efficiency for both cationic and anionic dyes suggests that these beads hold significant potential for the treatment of complex, real-world wastewater systems.

3.4. Adsorption isotherms

The adsorption isotherms of MB and MO onto PBC3.3@NaAlg beads were analyzed using the Langmuir,

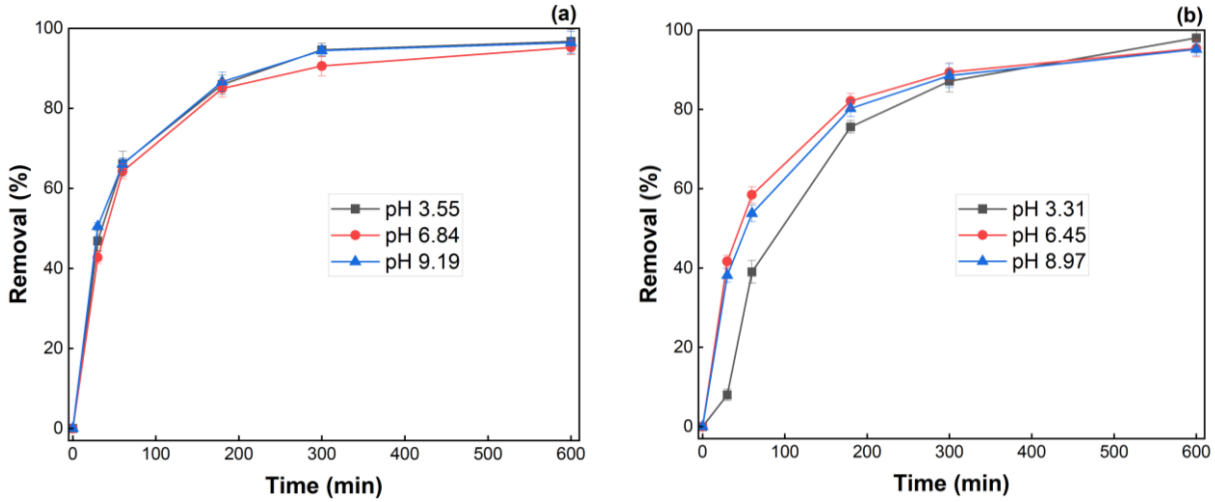

Fig. 6. Effect of initial pH solution on MB (a) and MO (b) adsorption by PBC3.3@NaAlg bead. Experimental parameters: $[MB]_{inital}$ = 300 mg/L and $[MO]_{inital}$ = 400 mg/L

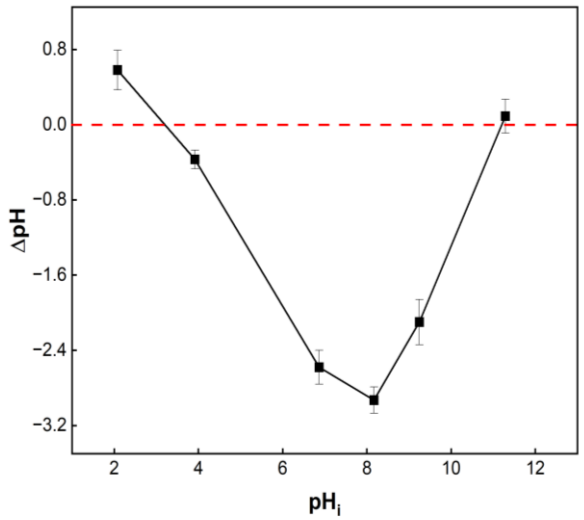

Fig. 7. Point of zero charge of PBC3.3@NaAlg beads

Freundlich, Temkin, and Dubinin-Radushkevich (D-R) models, with the results and corresponding fitting parameters illustrated in Fig. 8 and Table 3. The experimental data for dyes demonstrated an excellent fit with the Langmuir model, yielding adjusted correlation coefficients (*adj.*R^2) of 0.9781 and 0.9761 for MB and MO, respectively. This strong correlation signifies a predominant monolayer adsorption process on a homogeneous bead surface, where a finite number of identical active sites are homogeneously distributed on the adsorbent surface without any lateral interaction between the adsorbed molecules. There are a fixed number of identical active sites on the surface, and each site can hold only one dye molecule. Once all these sites are filled, the surface becomes saturated, and no more dye can be adsorbed. Furthermore, the dimensionless separation factor (R_L) remained within the $0 < R_L < 1$ range, confirming the favorable nature of the adsorption (Al-Ghouti and Da'ana 2020). Based on the Langmuir model, the maximum adsorption capacities (q_{max}) were determined to be 279.68 mg/g for MB and 179.02 mg/g for MO. Although the Freundlich heterogeneity factors ($1/n_F$) were 0.39 and 0.40, suggesting a theoretically heterogeneous surface ($0 < 1/n_F < 1$) (Ohemeng-Boahen *et al.* 2019), the lower *adj.* R^2 values (0.9153 and 0.9533) compared to the Langmuir model indicate that the surface sites are more functionally homogeneous. Regarding the adsorbate-adsorbent interactions, the Temkin model provided a moderate fit (*adj.*R^2 of 0.9305 and 0.9616), implying that the interaction plays a role in the adsorption mechanism. Conversely, the poor fit of the D-R model (*adj.* R^2 = 0.8242 for MB and 0.7029 for MO) suggests that micropore volume filling is not the governing mechanism. Based on this model, the calculated free energies ($E < 8$ kJ/mol) characterize the process as predominantly physisorption.

3.5. Thermodynamics studies

The thermodynamic behavior of MB and MO adsorption onto the composite was systematically evaluated through the calculated parameters of Gibbs free energy ΔG^0, enthalpy ΔH^0, and entropy ΔS^0 (Table 4). Across the investigated temperature

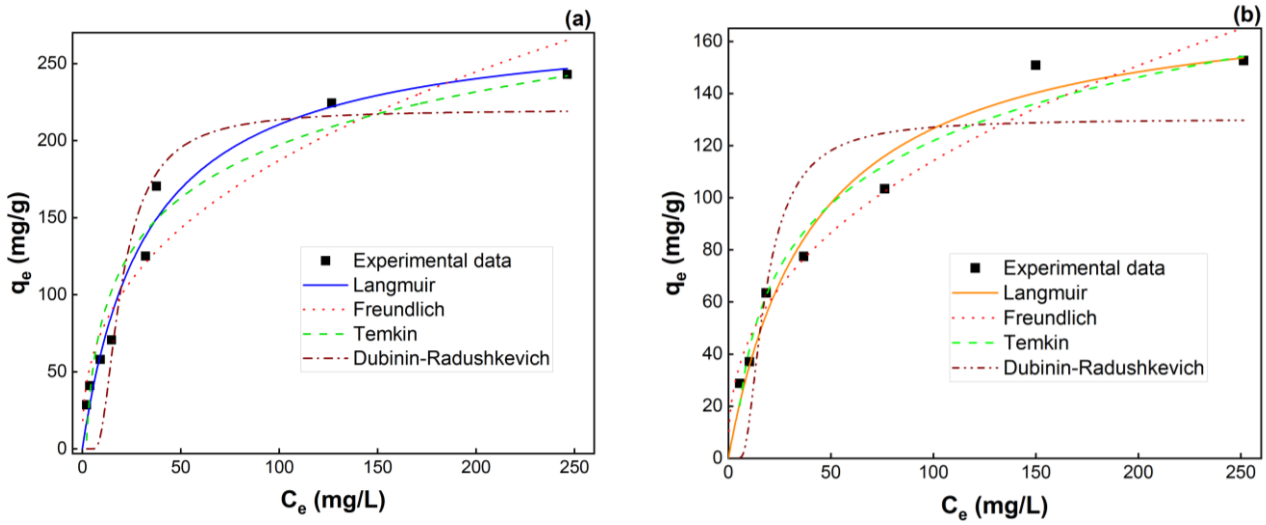

Fig. 8. Adsorption isotherm data and fitted models of MB (a) and MO (b) on PBC3.3@NaAlg bead

Table 3.
Isotherms model parameters derived from experimental data

Isotherm Model	Model Parameters		MB		MO	
	Symbol	Unit	Value	Adj.R^2	Value	Adj.R^2
Langmuir	q_{max}	mg/g	279.68±15.92	0.9781	179.02±11.39	0.9761
	K_L	L/mg	0.030±0.005		0.024±0.004	
	R_L	-	0.143-0.016		0.172-0.02	
Freundlich	K_F	(mg/g)(L/mg)$^{1/n}$	31.60±7.94	0.9153	18.06±3.79	0.9533
	$1/n_F$	-	0.39		0.40	
Temkin	a_T	L/g	0.53±0.16	0.9305	0.32±0.07	0.9616
	b_T	J/mol	50.78		71.69	
Dubinin-Radushkevich	q_{DR}	mg/g	220.14±22.67	0.8242	130.25±15.46	0.7029
	K_{DR}	mol^2/KJ^2	303.58±121.79		250.15±128.34	
	E	kJ/mol	0.041		0.045	

Table 4.
Thermodynamic parameters for the sorption of MB and MO onto PBC3.3@NaAlg beads

T (K)	MB			MO		
	ΔG (kJ/mol)	ΔH (kJ/mol)	ΔS (J/mol.K)	ΔG (kJ/mol)	ΔH (kJ/mol)	ΔS (J/mol.K)
303	-3.310			-3.338		
313	-3.667	7.489	35.642	-3.655	6.234	31.593
323	-4.023			-3.971		

range from 303 K to 323 K, the negative values of ΔG^0 for both dye systems signify that the adsorption process is highly spontaneous and energetically favorable. Notably, the magnitude of ΔG^0 becomes increasingly negative with rising temperatures, shifting from -3.310 to -4.023 kJ/mol for MB and from -3.338 to -3.971 kJ/mol for MO, which indicates that elevated temperatures enhance the adsorption efficiency. This endothermic nature is validated by the positive enthalpy changes of 7.489 kJ/mol for MB and 6.234 kJ/mol for MO. Furthermore, since these ΔH^0 values safely below the typical threshold of 20 kJ/mol, it can be inferred that the binding pathway is predominantly governed by physisorption interactions, including electrostatic forces, weak intermolecular attractions, and hydrogen bonding. Concurrently, the positive entropy changes ΔS^0 of 35.642 J/(mol.K) for MB and 31.593 J/(mol.K) for MO reflect an augmented degree of randomness at the solid-liquid interface. The increase in system disorder mainly results from the displacement of water molecules from the adsorbent surface during dye binding.

3.6. Adsorption kinetic studies

To elucidate the mechanisms and dynamic behavior governing the adsorption of MB and MO onto PBC3.3@NaAlg beads, the experimental data were analyzed using pseudo-first-order (PFO), pseudo-second-order (PSO), Elovich, and intraparticle diffusion models. The model results and calculated parameters are shown in Fig. 9 and Table 5. The fitness of models could be estimated based on the R^2 values. In general, the data obtained about MB and MO removed by PBC3.3@NaAlg beads

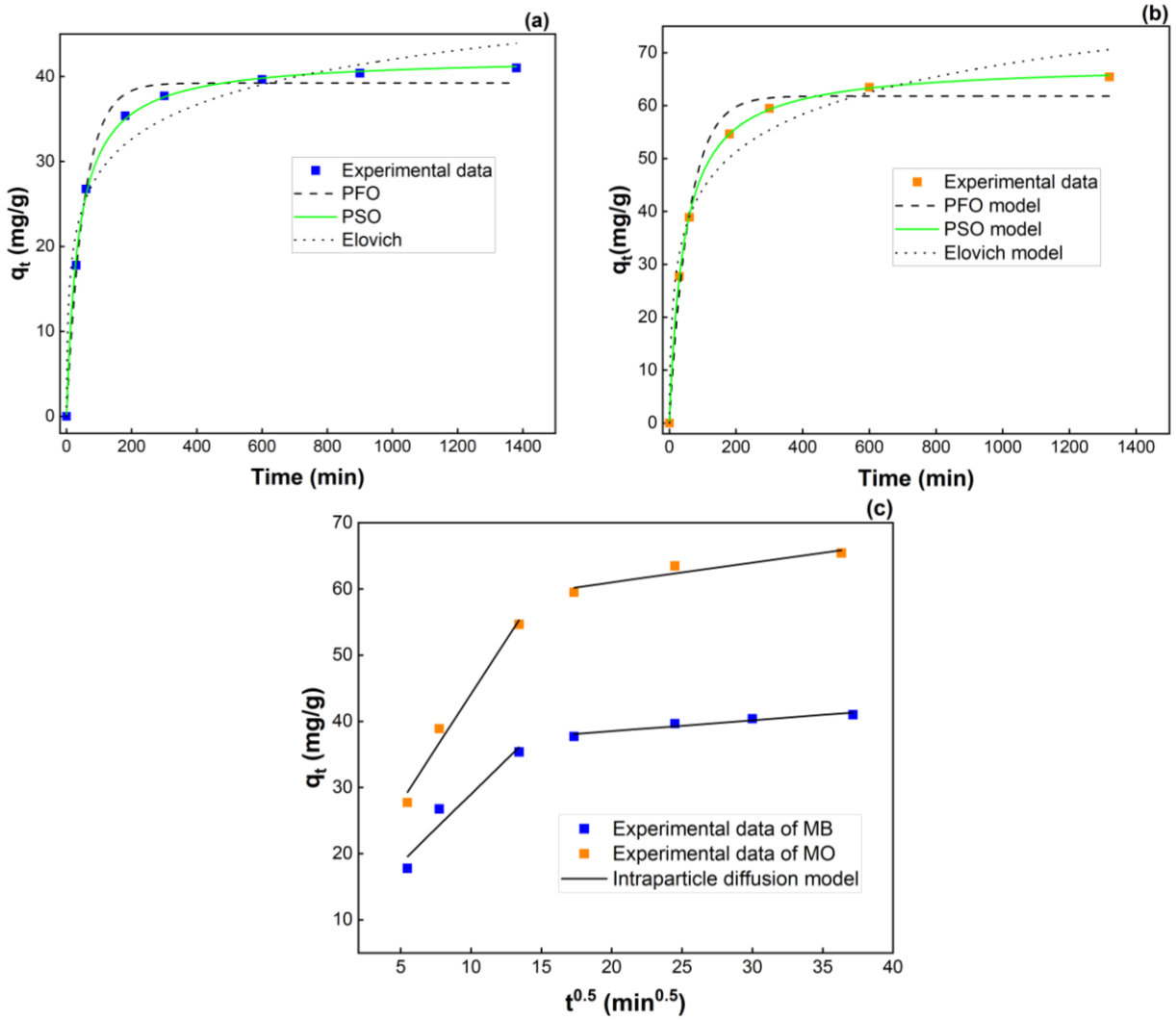

Fig. 9. Sorption kinetic studies of MB and MO on PBC3.3@NaAlg bead fitted by: (**a**) PFO, PSO, and Elovich models and (**b**) intraparticle diffusion model

Table 5.
Adsorption kinetic parameters of MB and MO on PBC3.3@NaAlg beads

Kinetic model	Parameter	Unit	MB	MO
PFO	$q_{e,cal}$	mg/g	39.23	61.82
	$q_{e,exp}$	mg/g	41.01	65.43
	R^2	-	0.9906	0.9861
PSO	$q_{e,cal}$	mg/g	42.31	67.93
	$q_{e,exp}$	mg/g	41.01	65.43
	R^2	-	0.9988	0.9999
Elovich				7.4056
	α	mg/g.min	7.8048	
	β	g/mg	0.1713	0.0970
	R^2	-	0.9696	0.9755
Intraparticle diffusion	$k_{d,1}$	mg/g.min$^{0.5}$	2.08	3.27
	R^2	-	0.9365	0.9793
	$k_{d,2}$	mg/g.min$^{0.5}$	0.16	0.30
	R^2	-	0.9269	0.8912

were well fitted with PFO, PSO, and Elovich models (R^2 > 0.95). Among these models, the PSO model provided the most superior fit (R^2 > 0.99). The high degree of convergence between the calculated adsorption capacities ($q_{e,cal}$) and the experimental values ($q_{e,exp}$) in the PSO model indicates that the process is often associated with chemisorption (Wang and Guo 2020). To better understand the rate-controlling step, the intraparticle diffusion model from Fig. 9c was evaluated. Specifically, the intraparticle diffusion plot displays a multi-stage process where the initial sharp phase represents the boundary layer effect, where dye molecules diffuse through the liquid film onto the external surface. The subsequent slower phase corresponds to the intraparticle or pore diffusion stage, where the molecules penetrate the internal porous network of the adsorbent. The fact that the regression lines do not pass through the origin confirms that intraparticle diffusion is involved but is not the sole rate-limiting step. Instead, both film diffusion and chemical interactions collectively control the overall adsorption rate. Given the relatively lower fit of this model compared to other models, it can be concluded that the overall sorption kinetics are not solely governed by intraparticle diffusion, although it still plays a significant role in the multi-stage transport process (Chen *et al.* 2021).

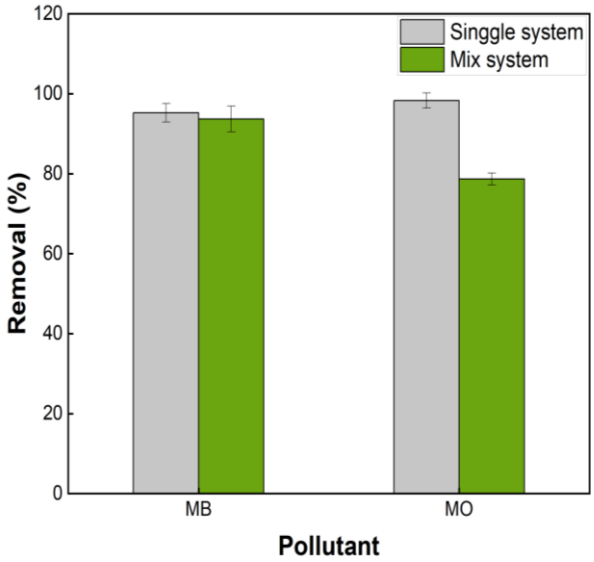

Fig. 10. Adsorption efficiency of MB and MO in single and binary mixed systems

3.7 Competitive adsorption behavior of MB and MO

The competitive adsorption behaviors of MB and MO were evaluated by comparing their removal efficiencies in both single and binary systems (Fig. 10). In the single-component systems, the adsorbent exhibited exceptional affinity toward both dyes, achieving high removal efficiencies exceeding 95% for MB and 98% for MO. However, a noticeable decline in the removal percentage was observed in the binary mixed system, particularly for MO, whose removal efficiency dropped significantly to approximately 78.68%. This decrease is due to competitive adsorption, as both dye molecules compete for the limited active sites on the adsorbent surface. MB's higher removal efficiency (93.67%) in the mixture indicates its superior competitiveness over MO, which is attributed to stronger electrostatic attraction, preferential orientation, or better structural fitting. Consequently, despite the competitive interference between the dyes, the material maintains high removal efficiency in both single and mixed systems, demonstrating its strong potential for real wastewater treatment.

3.8. Performance comparison of PBC3.3@NaAlg beads with the literature

To evaluate the adsorption performance of the synthesized PBC3.3@NaAlg beads, their maximum adsorption capacities for MB and MO were compared with those of various hydrogel-based adsorbents in the literature. As presented in Table 6, the PBC3.3@NaAlg beads exhibited highly competitive adsorption capacities of 279.68 mg/g for MB and 179.02 mg/g for MO. Notably, the MB uptake of PBC3.3@NaAlg beads significantly outperformed several recent biopolymer hydrogels, including rabbit skin-gelatin beads (185.55 mg/g) and grafted natural melanin κ-carrageenan hydrogel beads (48.63 mg/g). Furthermore, while most reported materials targeted only a single class of dyes, our developed beads demonstrated a distinct dual-functional advantage by efficiently capturing both cationic (MB) and anionic (MO) dyes. This broad-spectrum removal capability, combined with the utilization of eco-friendly and low-cost pomelo peel biochar, underscores the superior potential of PBC3.3@NaAlg beads for flexible wastewater remediation.

Table 6.
Comparative study of dye adsorption capacity for different hydrogel beads

Different hydrogel beads	Dye	Adsorption capacity (mg/g)	References
Rabbit skin-gelatin beads	MB	185.55	(Zhang et *al.* 2022)
	Basic fuchsin	271.01	
Walnut shell biochar-based composite hydrogel	MB	1494	(Li *et al.* 2024)
	Malachite green	1182	
	Neutral Red	1031.6	
Chitosan-montmorillonite hydrogel beads	Methyl green	300	(Kurczewska 2022)
Multifunctional carboxymethyl cellulose-dextran	Basic red 46	344.82	(Benhalima *et al.* 2024)
Sulfate/AgNPs@zeolite hydrogel beads	MB	454.55	
Sodium alginate-guar-gum-tannic acid based nanocomposite hydrogel beads	Malachite green	203	(Rather *et al.* 2023)
Chitosan-Lignin hydrogel beads	DB-218	93.5	(Bashir *et al.* 2025)
Grafted natural melanin κ-carrageenan hydrogel bead	MB	48.63	(Hao *et al.* 2023)
	Malachite green	37.84	
Fly ash composite hydrogel	MO	226.16	(Zari *et al.* 2025)
PBC3.3@NaAlg beads	MB	279.68	This study
	MO	179.02	

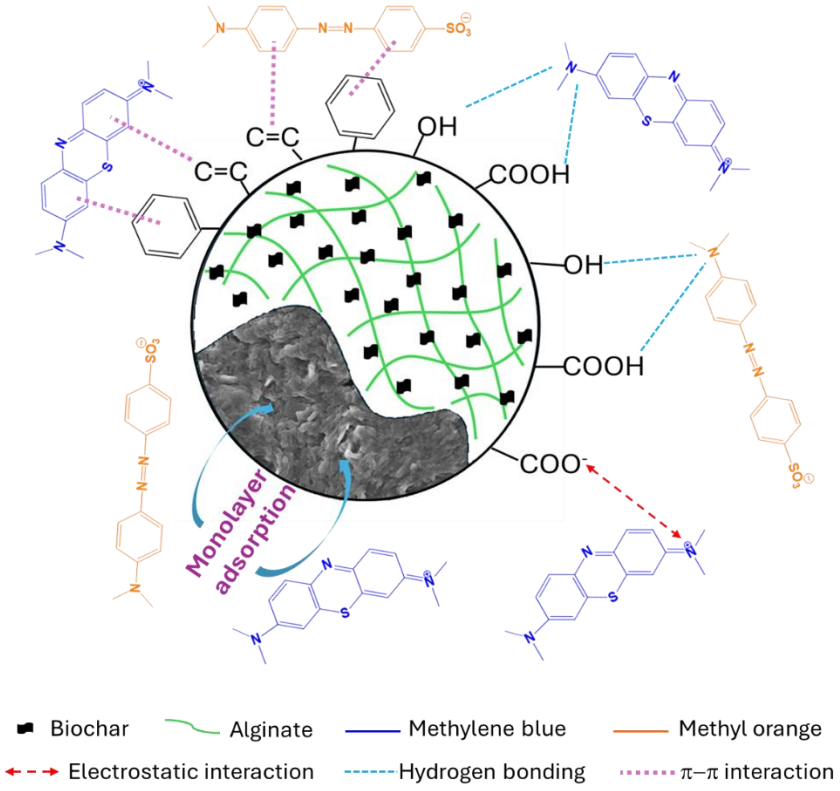

Fig. 11. Possible removal mechanism of MB and MO on PBC3.3@NaAlg

3.9. Possible mechanism

Based on the aforementioned analysis, the removal of MB and MO by the composite beads is governed by a synergistic mechanism involving hydrogen bonding, π–π interactions, and electrostatic forces (Fig. 11). The presence of micro-sheets on the bead surface, as revealed by morphological characterization, facilitates the entrapment and subsequent migration of dye molecules into the porous network to form monolayer adsorption. The structure of the activated biochar, rich in carboxylate and hydroxyl functional groups, enables the formation of hydrogen bonds with the nitrogen and oxygen atoms of the dye molecules. Furthermore, π–π stacking interactions occur between the delocalized π-electron system, the biochar's graphitic layers, and the aromatic rings of the MB and MO molecules. This is corroborated by FT-IR spectra (Fig. 3), where shifts in the vibrational peaks of -OH, -COOH, and C=C groups (Table 2) post-adsorption validate the involvement of both hydrogen bonding and π–π interactions. Although direct quantification of these forces is limited, the observed peak shifts and intensity variations provide strong indirect evidence supporting the proposed mechanism. The electrostatic interaction between dye and bead is not significant as the results obtained in the effect of initial pH solution (Fig. 6). In the case of MB adsorption, this interaction could happen between the negatively charged carboxylate groups of the alginate matrix and the cationic MB molecules, as indicated by a slight removal of MB by NaAlg beads. To sum up, MB and MO were taken up by a hybrid of physisorption and

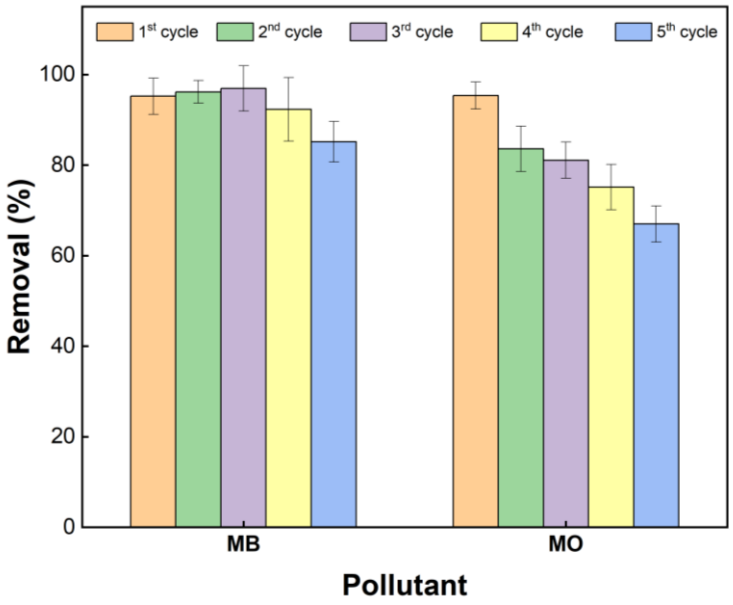

Fig. 12. The reusability of PBC3.3@NaAlg beads for MB and MO adsorption. Experimental parameters: $[MB]_{inital}$ = 300 mg/L, $[MO]_{inital}$ = 400 mg/L, and $t_{adsorption}$ = 600 min

chemisorption. It was initiated by the diffusion of dyes into the pores, followed by robust interaction with active sites across the external and internal bead architectures.

3.10 Regeneration of PBC3.3@NaAlg beads

To assess the adsorbent's reusability, five consecutive adsorption-desorption cycles were performed using ethanol 70° as the eluting agent for both MB and MO. As illustrated in Fig. 12, the removal efficiency for MB remained remarkably high and stable, maintaining over 95% efficiency up to the 3rd cycle and dropping only slightly to approximately 85% by the 5th cycle. Conversely, the removal of MO exhibited a gradual decline, decreasing from an initial 95.36% to 67.12% in the final round. This performance in MO adsorption is likely dictated by steric factors; specifically, the smaller molecular size of MO may facilitate deeper penetration into the internal pore network, leading to incomplete elution during the regeneration phase. Nevertheless, the sustained high removal efficiencies for both dyes under continuous operation suggest that this method represents a potent and commercially viable strategy for the remediation of dye-laden industrial wastewater. Furthermore, the insets in SEM images (Fig. 4) confirm that the spent beads successfully retain their spherical shape and macro-structural integrity, thereby demonstrating excellent mechanical durability and stability against degradation throughout the five successive runs.

4. Conclusions

The successful synthesis of this hybrid material demonstrates that biochar can be effectively embedded within a sodium alginate polymeric matrix, resulting in a composite characterized by a complex lamellar morphology and a heterogeneous internal architecture of distinct micro-sheets. Insights from FTIR spectroscopy reveal a high density of diverse surface functional groups, which act as active sites to significantly boost the sequestration of both methylene blue and methyl orange. A key advantage of this adsorbent is its exceptional stability, as it maintains high removal efficiency across a wide pH spectrum ranging from 3.0 to 9.0. Furthermore, comprehensive isotherm and kinetic studies indicate that the removal process operates through a multifaceted dual-action mechanism, combining physical diffusion into the porous network with robust chemical interactions on the surface. By immobilizing fine biochar particles within a macroscopic hydrogel scaffold, the composite effectively resolves common industrial hurdles related to the separation and recovery of powdered adsorbents. Ultimately, its proven effectiveness in treating both cationic and anionic dyes during continuous flow operations highlights its significant promise for large-scale, practical wastewater treatment applications.

Acknowledgments

The author sincerely thanks the Institute of Environmental Science, Engineering and Management, Industrial University of Ho Chi Minh City for facilitating facilities and equipment to help complete this study.

Funding: The author did not receive support from any organization for the submitted work.

Competing Interests: The author has no relevant financial or non-financial interests to disclose.

Author Contributions: All authors contributed to the study conception and design. Material preparation, data collection, and analysis were performed by Tran ML. The first draft and previous versions of the manuscript were written by Tran ML.

Availability of data and materials: Data is available upon request.

Ethical Approval: No ethical approval was required for this study as it did not involve human or animal subjects.

Consent to participate: No human subjects were involved in this research.

Consent to publish: This study does not involve human participants or the collection of personal data.

References

Agarwala, R. & Mulky, L. (2023). Adsorption of dyes from wastewater: A comprehensive review. *ChemBioEng Reviews, 10*(3), 326-335. https://doi.org/10.1002/cben.202200011.

Akter, T., Protity, A.T., Shaha, M., Al Mamun, M., & Hashem, A. (2023). *The impact of textile dyes on the environment. Nanohybrid materials for treatment of textiles dyes*, Springer: 401-431.

Al-Asadi, S.T., Mussa, Z.H., Al-Qaim, F.F., Kamyab, H., Al-Saedi, H.F.S., Deyab, I.F., & Kadhim, N.J. (2025). A comprehensive review of methylene blue dye adsorption on activated carbon from edible fruit seeds: A case study on kinetics and adsorption models. *Carbon Trends, 20*, 100507. https://doi.org/10.1016/j.cartre.2025.100507.

Al-Gheethi, A.A., Azhar, Q.M., Kumar, P.S., Yusuf, A.A., Al-Buriahi, A.K., Mohamed, R.M.S.R., & Al-Shaibani, M.M. (2022). Sustainable approaches for removing Rhodamine B dye using agricultural waste adsorbents: A review. *Chemosphere, 287*, 132080. https://doi.org/10.1016/j.chemosphere.2021.132080.

Al-Ghouti, M.A. & Da'ana, D.A. (2020). Guidelines for the use and interpretation of adsorption isotherm models: A review. *Journal of hazardous materials, 393*, 122383. https://doi.org/10.1016/j.jhazmat.2020.122383.

Al-Tohamy, R., Ali, S.S., Li, F., Okasha, K.M., Mahmoud, Y.A.G., Elsamahy, T., Jiao, H., Fu, Y., & Sun, J. (2022). A critical review on the treatment of dye-containing wastewater: Ecotoxicological and health concerns of textile dyes and possible remediation approaches for environmental safety. *Ecotoxicology and environmental safety, 231*, 113160. https://doi.org/10.1016/j.ecoenv.2021.113160.

Bal, G. & Thakur, A. (2022). Distinct approaches of removal of dyes from wastewater: A review. *Materials Today: Proceedings, 50*, 1575-1579. https://doi.org/10.1016/j.matpr.2021.09.119.

Bashir, T., Dutta, J., Masarat, S., Rafatullah, M., Asthana, N., Khan, A.A., & Fatima, S. (2025). Application of novel Chitosan-Lignin hydrogel beads for optimized removal of textile dye DB-218. *Journal of Molecular Structure*, 1324, 140892. https://doi.org/10.1016/j.molstruc.2024.14089.

Bellaj, M., Aziz, K., El Achaby, M., El Haddad, M., Gebrati, L., Kurniawan, T.A., Chen, Z., Yap, P.S., & Aziz, F. (2024). Cationic and anionic dyes adsorption from wastewater by clay-chitosan composite: an integrated experimental and modeling study. *Chemical Engineering Science, 285*, 119615. https://doi.org/10.1016/j.ces.2023.119615.

Benhalima, T., Sadi, A., Dairi, N., & Ferfera-Harrar, H. (2024). Multifunctional carboxymethyl cellulose-dextran sulfate/AgNPs@ zeolite hydrogel beads for basic red 46 and methylene blue dyes removal and water disinfection control. *Separation and Purification Technology,* 342, 127001. https://doi.org/10.1016/j.seppur.2024.127001.

Biswas, S., Mohapatra, S.S., Kumari, U., Meikap, B.C., & Sen, T.K. (2020). Batch and continuous closed circuit semi-fluidized bed operation: Removal of MB dye using sugarcane bagasse biochar and alginate composite adsorbents. *Journal of Environmental Chemical Engineering*, 8, 103637. https://doi.org/10.1016/j.jece.2019.103637.

Chen, J., Ouyang, J., Cai, X., Xing, X., Zhou, L., Liu, Z., & Cai, D. (2021). Removal of ciprofloxacin from water by millimeter-sized sodium alginate/H_3PO_4 activated corncob-based biochar composite beads. *Separation and Purification Technology, 276*, 119371. https://doi.org/10.1016/j.seppur.2021.119371.

Das, E., Rabha, S., Talukdar, K., Goswami, M., & Devi, A. (2023). Propensity of a low-cost adsorbent derived from agricultural wastes to interact with cationic dyes in aqueous solutions. *Environmental Monitoring and Assessment, 195*(9), 1044. https://doi.org/10.1007/s10661-023-11656-1.

Faried, M., Shameli, K., Miyake, M., Zakaria, Z., Hara, H., Khairudin, N., & Etemadi, M. (2016). Ultrasound-assisted in the synthesis of silver nanoparticles using sodium alginate mediated by green method. *Digest Journal of Nanomaterials and Biostructures, 11*(2), 547-552.

Haleem, A., Shafiq, A., Chen, S.Q., & Nazar, M. (2023). A comprehensive review on adsorption, photocatalytic and chemical degradation of dyes and nitro-compounds over different kinds of porous and composite materials. *Molecules, 28*(3), 1081. https://doi.org/10.3390/molecules28031081.

Hao, R., Ji, H., Gao, L., Chen, J., Shi, Y., Yang, J., & Yuan, C. (2023). Grafted natural melanin κ-carrageenan hydrogel bead adsorbents: New strategy for bioremediation of cationic dye contamination in aqueous solutions. *Chemical Engineering Research and Design*, 199, 1-10. https://doi.org/10.1016/j.cherd.2023.09.016.

Haque, A.N.M.A., Sultana, N., Sayem, A.S.M., & Smriti, S.A. (2022). Sustainable adsorbents from plant-derived agricultural wastes for anionic dye removal: a review. *Sustainability, 14*(17), 11098. https://doi.org/10.3390/su141711098.

Hosny, N.M., Gomaa, I., & Elmahgary, M.G. (2023). Adsorption of polluted dyes from water by transition metal oxides: A review. *Applied Surface Science Advances, 15*, 100395. https://doi.org/10.1016/j.apsadv.2023.100395.

Islam, T., Repon, M.R., Islam, T., Sarwar, Z., & Rahman, M.M. (2023). Impact of textile dyes on health and ecosystem: a review of structure, causes, and potential solutions. *Environmental Science and Pollution Research, 30*(4), 9207-9242. https://doi.org/10.1007/s11356-022-24398-3.

Jorge, A.M., Athira, K., Alves, M.B., Gardas, R.L., & Pereira, J.F. (2023). Textile dyes effluents: A current scenario and the use of aqueous biphasic systems for the recovery of dyes. *Journal of Water Process Engineering, 55*, 104125. https://doi.org/10.1016/j.jwpe.2023.104125.

Kathing, C. & Saini, G. (2022). A review of various treatment methods for the removal of dyes from textile effluent. *Recent Progress in Materials, 4*(4), 1-15. https://doi.org/10.21926/rpm.2204028.

Kumari, H., Sonia, Suman, Ranga, R., Chahal, S., Devi, S., Sharma, S., Kumar, S., Kumar, P., & Kumar, S. (2023). A review on photocatalysis used for wastewater treatment: dye degradation. *Water, Air, & Soil Pollution, 234*(6), 349. https://doi.org/10.1007/s11270-023-06359-9.

Kurczewska, J. (2022). Chitosan-montmorillonite hydrogel beads for effective dye adsorption. *Journal of Water Process Engineering*, 48, 102928. https://doi.org/10.1016/j.jwpe.2022.102928.

Li, K., Wu, J., Li, X., Li, B., & Zhou, D. (2024). Preparation of porous composite hydrogel with ultra-high dye adsorption capacity based on biochar: Adsorption behaviors and mechanisms. *Chemical Engineering Science, 295*, 120115. https://doi.org/10.1016/j.ces.2024.120115.

Liao, J., Li, Y., Li, H., Liu, J., Xie, Y., Wang, J., & Zhang, Y. (2018). Preparation, bioactivity and mechanism of nano-hydroxyapatite/sodium alginate/chitosan bone repair material. *Journal of applied biomaterials & functional materials, 16*(1), 28-35.

Lin, J., Ye, W., Xie, M., Seo, D.H., Luo, J., Wan, Y., & Van der Bruggen, B. (2023). Environmental impacts and remediation of dye-containing wastewater. *Nature Reviews Earth & Environment, 4*(11), 785-803. https://doi.org/10.1038/s43017-023-00489-8.

Liu, Q. (2020). Pollution and treatment of dye waste-water. IOP conference series: earth and environmental science, iop publishing. https://doi.org/10.1088/1755-1315/514/5/052001.

Lu, C., Yang, J., Khan, A., Yang, J., Li, Q., & Wang, G. (2022). A highly efficient technique to simultaneously remove acidic and basic dyes using magnetic ion-exchange microbeads. *Journal of Environmental Management, 304*, 114173. https://doi.org/10.1016/j.jenvman.2021.114173.

Lu, H., Butler, J.A., Britten, N.S., Venkatraman, P.D., & Rahatekar, S.S. (2021). Natural antimicrobial nano composite fibres manufactured from a combination of alginate and oregano essential oil. *Nanomaterials, 11*(8), 2062. https://doi.org/10.3390/nano11082062.

Maheshwari, K., Agrawal, M., & Gupta, A.B. (2021). *Dye pollution in water and wastewater. Novel materials for dye-containing wastewater treatment*, Springer, 1-25.

Makarova, A.O., Derkach, S.R., Khair, T., Kazantseva, M.A., Zuev, Y.F., & Zueva, O.S. (2023). Ion-induced polysaccharide gelation: Peculiarities of alginate egg-box association with different divalent cations. *Polymers, 15*(5), 1243. https://doi.org/10.3390/polym15051243.

Nayagam, J.O.P. & Prasanna, K. (2022). Utilization of shell-based agricultural waste adsorbents for removing dyes: A review. *Chemosphere, 291*, 132737. https://doi.org/10.1016/j.chemosphere.2021.132737.

Ohemeng-Boahen, G., Sewu, D.D., & Woo, S.H. (2019). Preparation and characterization of alginate-kelp biochar composite hydrogel bead for dye removal. *Environmental Science and Pollution Research, 26*(32), 33030-33042. https://doi.org/10.1007/s11356-019-06421-2.

Rather, R.A., Bhat, M.A., & Shalla, A.H. (2023). Development of sodium alginate-guar-gum-tannic acid based nanocomposite hydrogel beads for removal of malachite green dye. *Materials Today Communications*, 36, 106358. https://doi.org/10.1016/j.mtcomm.2023.106358.

Rathi, B.S. & Kumar, P.S. (2022). Sustainable approach on the biodegradation of azo dyes: a short review. *Current Opinion in Green and Sustainable Chemistry, 33*, 100578. https://doi.org/10.1016/j.cogsc.2021.100578.

Saravanan, P., Josephraj, J., Thillainayagam, B.P., Ravindiran, G. (2023). Evaluation of the adsorptive removal of cationic dyes by greening biochar derived from agricultural bio-waste of rice husk. *Biomass Conversion and Biorefinery, 13*(5), 4047-4060. https://doi.org/10.1007/s13399-021-01415-y.

Shi, Y., Chang, Q., Zhang, T., Song, G., Sun, Y., & Ding, G. (2022). A review on selective dye adsorption by different mechanisms. *Journal of Environmental Chemical Engineering, 10*(6), 108639. https://doi.org/10.1016/j.jece.2022.108639.

Solayman, H., Hossen, M.A., Abd Aziz, A., Yahya, N.Y., Leong, K.H., Sim, L.C., Monir, M.U., & Zoh, K.D. (2023). Performance evaluation of dye wastewater treatment technologies: A review. *Journal of Environmental Chemical Engineering, 11*(3), 109610. https://doi.org/10.1016/j.jece.2023.109610.

Soltani, A., Faramarzi, M., & Mousavi Parsa, S.A. (2021). A review on adsorbent parameters for removal of dye products from industrial wastewater. *Water Quality Research Journal, 56*(4), 181-193. https://doi.org/10.2166/wqrj.2021.023.

Stachowiak, N., Kowalonek, J., Kozlowska, J., & Burkowska-But, A. (2023). Stability studies, biodegradation tests, and mechanical properties of sodium alginate and gellan gum beads containing surfactant. *Polymers, 15*(11), 2568. https://doi.org/10.3390/polym15112568.

Subrahmanya, T., Widakdo, J., Mani, S., Austria, H.F.M., Hung, W.S., HK, M., Nagar, J.K., Hu, C.C., & Lai, J.Y. (2022). An eco-friendly and reusable syringe filter membrane for the efficient removal of dyes from water via low pressure filtration assisted self-assembling of graphene oxide and SBA-15/PDA. *Journal of Cleaner Production, 349*, 131425. https://doi.org/10.1016/j.jclepro.2022.131425.

Tran, M.L. (2025). One-step preparation of activated pomelo peel biochar by using H_3PO_4 for removal of methylene blue: performance, isotherm, and kinetic studies. *Biomass Conversion and Biorefinery, 15*(7), 10305-10317. https://doi.org/10.1007/s13399-024-05848-z.

Tran, M.L., Nguyen, C.H., Tran, T.T.V., & Juang, R.S. (2025). One-step facile synthesis of pomelo peel biochar activated by KOH under air atmosphere for adsorptive removal of methylene blue and oxytetracycline. *Journal of Chemical Technology & Biotechnology*, 100, 1335-1345. https://doi.org/10.1002/jctb.7865.

Wang, J. & Guo, X. (2020). Adsorption kinetic models: Physical meanings, applications, and solving methods. *Journal of Hazardous materials, 390*, 122156. https://doi.org/10.1016/j.jhazmat.2020.122156.

Wu, S., Shi, W., Li, K., Cai, J., Xu, C., Gao, L., Lu, J., & Ding, F. (2023). Chitosan-based hollow nanofiber membranes with polyvinylpyrrolidone and polyvinyl alcohol for efficient removal and filtration of organic dyes and heavy metals. *International Journal of Biological Macromolecules, 239*, 124264. https://doi.org/10.1016/j.ijbiomac.2023.124264.

Yagub, M.T., Sen, T.K., Afroze, S., & Ang, H.M. (2014). Dye and its removal from aqueous solution by adsorption: a review. *Advances in colloid and interface science, 209*, 172-184. https://doi.org/10.1016/j.cis.2014.04.002.

Zari, R., Rathi, T., Gomase, V., EL Kaim Billah, R., Alhamami, M.A., Algethami, J.S., & Jugade, R. (2025). Eco-friendly synthesis of sodium alginate modified zeolite from fly ash composite hydrogel for efficient removal of methyl orange from water: batch studies and RSM optimization. *International Journal of Environmental Analytical Chemistry*, 1-31. https://doi.org/10.1080/03067319.2025.2553751.

Zhang, Y., Wang, P., Hussain, Z., Zhang, H., Wang, H., Chang, N., & Li, F. (2022). Modification and characterization of hydrogel beads and its used as environmentally friendly adsorbent for the removal of reactive dyes. *Journal of Cleaner Production*, 342, 130789. https://doi.org/10.1016/j.jclepro.2022.130789.

Zhao, Q., Zhang, H., Zhao, X., Wang, X., Zhang, K., Binguo, Z., Wang, S., Wang, B., Guo, F., & Ma, Y. (2024). Sodium alginate-based biochar gel spheres: synthesis, structural analysis, and ofloxacin adsorption efficiency. *Materials Research Express*, 11, 125507. https://doi.org/10.1088/2053-1591/ad988d.